◆ ANNUAL ISSUE

EARLY CAREER SCHOLARS IN MATERIALS SCIENCE

Relaxor behavior and electrothermal properties of Sn- and Nb-modified (Ba,Ca)TiO₃ Pb-free ferroelectric

Sarangi Venkateshwarlu[1], Sanjib Nayak[1], Frederick P. Marlton[2], Florian Weyland[3], Nikola Novak[4], Deepam Maurya[5], Yashaswini Veerabhadraiah[1], Olaf Borkiewicz[6], Kevin A. Beyer[6], Mads R.V. Jørgensen[7], Abhijit Pramanick[1,a)]

[1]Department of Materials Science and Engineering, City University of Hong Kong, Hong Kong SAR, China
[2]Center for Materials Crystallography, Department of Chemistry and INANO, Aarhus University, Aarhus C 8000, Denmark
[3]Institute of Materials Science, Technische Universitat Darmstadt, Darmstadt 64287, Germany
[4]Department of Condensed Matter Physics, Institute Jožef Stefan, Ljubljana 1000, Slovenia
[5]Department of Materials Science and Engineering, Virginia Tech, Blacksburg, VA 24061, USA
[6]Advanced Photon Source, Argonne National Laboratory, Lemont, IL 60439, United States of America
[7]Center for Materials Crystallography, Department of Chemistry and INANO, Aarhus University, 8000 Aarhus C, Denmark; and MAX IV Laboratory, Lund University, SE-221 00 Lund, Sweden
a)Address all correspondence to this author. e-mail: abhijit.pramanick@gmail.com
This paper has been selected as an Invited Feature Paper.

Relaxor ferroelectrics have drawn attention for possible applications in solid-state cooling and thermal energy harvesting, owing to their electrothermal energy conversion properties. Here, we have synthesized and characterized the structure–property correlations of a new Sn- and Nb-doped (Ba,Ca)TiO₃ relaxor ferroelectric with large pyroelectric and electrocaloric effects over a broad temperature range. We observed two peaks for the temperature-dependent pyroelectric coefficient: (i) $-(\partial P/\partial T) \sim 563$ μC/(m² K) at $T \sim 270$ K and (ii) $-(\partial P/\partial T) \sim 1021$ μC/(m² K) at $T \sim 320$ K. In addition, a broad peak for electrocaloric temperature change is observed near 320 K with a relative cooling power of ~17 J/kg. These properties could be correlated to structural changes observed using X-ray diffraction at two different temperature ranges in the material. Analysis of high-energy X-ray scattering and specific heat capacity data revealed a transition from the cubic to tetragonal phase near $T_m \sim 320$ K, whereas an additional increase in the tetragonality (c/a) of the polar phase is observed below $T_s \sim 270$ K.

Abhijit Pramanick

Abhijit Pramanick is an Assistant Professor at the City University of Hong Kong. He obtained his Bachelors in Engineering from the National Institute of Technology, India, and his Masters in Engineering from the Indian Institute of Science, Bangalore. He received his Ph.D. in Materials Science and Engineering in 2009 from the University of Florida, Gainesville, working under the mentorship of Prof. Jacob L Jones. After his Ph.D., he held a postdoctoral appointment in the research group of Prof. Scott Misture at the Alfred University in New York, USA. Subsequently, he moved to the Oak Ridge National Laboratory, where he spent three and half years working on the applications of different X-ray and neutron scattering techniques to understand the microscopic origins of functional responses in ferroelectric and ferromagnetic materials. He has coauthored more than 40 publications. For his work on in situ structural characterization of ferroelectric ceramics using X-ray diffraction, he was awarded the prestigious Edward C. Henry Award by the American Ceramic Society in the years 2010 and 2012. His current research group at City University of Hong Kong focuses on synthesis and characterization of structure–property correlations of advanced ceramic and polymeric materials for application in smart and energy technologies.

Introduction

Relaxor ferroelectrics (or relaxors in short) are among the most successful electronic ceramics because of their highly attractive dielectric, piezoelectric, pyroelectric, and electrocaloric properties [1, 2, 3, 4, 5]. In addition, fundamental understanding of their physicochemical nature has drawn much attention because of various fascinating properties, such as a strong frequency-dependent maximum permittivity temperature (T_M),

deviation from Curie–Weiss law for ferroelectric phase transition, relatively large $\partial P/\partial T$ over a broad temperature range, and a large electromechanical response [5, 6, 7, 8]. The behavior of relaxors can be generally attributed to the presence of nanoscale polar clusters with correlated atomic disorder [9, 10], and in this regard, relaxors can be broadly compared with spin glasses and dipolar glasses [11, 12]. Lead (Pb)-based ABO_3 perovskites, with the general formula of $Pb\left(B'^{2+}_{1/3}B''^{5+}_{2/3}\right)O_3$ (B'^{2+} = Mg, Co, Ni, Zn; B''^{5+} = Nb, Ta) and their solid solutions with prototypical ferroelectric $PbTiO_3$, are the most studied and technologically important relaxor ferroelectrics [13]. However, due to the negative environmental concerns surrounding the presence of Pb, design of new Pb-free relaxors has developed into an important research endeavor in materials science [14]. In this regard, investigation of Pb-free compounds with similar structural characteristics to Pb-based relaxors is a promising approach toward developing new functional materials.

One salient feature of Pb-based relaxors is the existence of cooperative multisite atomic displacements, which are correlated over only nanometer length scales. The cooperative atomic displacements can be understood based on the classical picture provided for $Pb\left(B'^{2+}_{1/3}B''^{5+}_{2/3}\right)O_3$ relaxors [15, 16]. In this model, the octahedral B-site is occupied by two sets of ions: B'^{2+} ions which are larger and ferroelectrically inactive, and B''^{5+} ions which are smaller and ferroelectrically active. For certain arrangements of the B'^{2+} and B''^{5+} ions, the intermediate oxygen ions can be forced to move toward B''^{5+}, which consequently induces a movement of the A-site cation (Pb^{2+} in this case) toward B'^{2+} to form three shorter Pb–O–B'^{2+} and three longer Pb–O–B''^{5+} bonds. In this manner, the off-centered displacements of the A-site and B-site ions toward or away from the intermediate oxygen ions can lead to large electrical dipoles. At the same time, a disordered arrangement of B'^{2+} and B''^{5+} ensures that the dipoles are correlated over only short distances. The type of cooperative atomic displacements in Pb-based ferroelectrics described above is aided by two factors: (a) hybridization between the empty B''^{5+} d-orbitals and the O^{2-} p-orbitals, which makes the B″–O bond ferroelectrically active in contrast to the inactive B′–O bond, and (b) the presence of lone pair electrons on Pb^{2+}, which favors the formation of shorter Pb–O bonds and thus accommodates the A-site displacements [15, 17]. Replication of these mechanisms for Pb-free chemistries can be a rational step for replacement of Pb in many electronic ceramics; nevertheless, such a possibility has not been systematically investigated.

In the present work, we have synthesized and characterized ceramics of a new composition, namely, Nb- and Sn-doped $(Ba,Ca)TiO_3$. $BaTiO_3$ is similar in structure to the prototype Pb-based ferroelectric $PbTiO_3$ near room temperature (RT), i.e., both compounds exhibit a tetragonal crystal structure with relatively large c/a ratio. However, there are significant differences between $BaTiO_3$ and the Pb-based ferroelectrics in terms of chemical bond formations [17, 18]. In Pb-based ABO_3 compounds, the lone-pair $6s$ electrons on the A-site Pb atoms hybridize strongly with the O-$2p$ orbitals, which reinforces cooperative atomic displacements. By contrast, the Ba–O bond in $BaTiO_3$ is more ionic in nature, which hinders the formation of shorter and longer A–O bonds. Nevertheless, A-site displacements in solid solutions of $BaTiO_3$ could be induced through various mechanisms. One such mechanism is quantum fluctuations, which can be introduced by forming a solid solution with ions of smaller radii. In this case, by substituting Ba^{2+} with Ca^{2+}, Ca^{2+} become off-centered along the $\langle 113 \rangle$ direction [19]. Another possibility is the stereochemical effect, which is introduced by incorporating small amounts of Sn^{2+} at the A site of $BaTiO_3$. Similar to Pb^{2+}, Sn^{2+} has a lone-pair of electrons, and thus it can be expected to increase A–O bond covalency and consequently lead to off-centered atomic displacements [20, 21]. Exclusive inclusion of Sn^{2+} onto the A site is however difficult because of disproportion of Sn^{2+} and Sn^{4+}. Here, it has to be noted that a natural distribution between the two oxidation states has been reported earlier [22, 23], and such a distribution can also be expected for Sn-doped (Ba,Ca) TiO_3 [24].

To induce cooperative atomic displacements as indicated in Fig. 1, we need to introduce different ions at the B site of $BaTiO_3$, which form bonds to oxygen with different degrees of covalency [15, 16]. As shown earlier by Cohen, hybridization between the empty d-orbitals of the transition metal ions and oxygen $2p$ states can form strong covalent bonds and stabilize ferroelectricity [17]. Here, Nb^{5+} is introduced at the B site to form stronger covalent bonds with oxygen. At the same time, Sn^{4+} at the B site is expected to form weakly covalent bonds because of lack of d and p orbitals' hybridization. In such a scenario, the larger O anions can be expected to move closer to Nb^{5+} ions and away from the Sn^{4+} ions, thereby facilitating the off-centered displacements of the A-site cations. The proposed mechanism is illustrated in Fig. 1.

Following the ideas outlined earlier, we successfully designed a solid solution composition of Nb- and Sn-doped $(Ba,Ca)TiO_3$ that exhibits relaxor-like properties with temperature for maximum permittivity (T_m) near RT. The relaxor-like properties of the material are confirmed from dielectric spectroscopy, specific heat capacity, and piezo force microscopy (PFM) measurements. The dielectric permittivity spectrum showed two anomalies, as evident from a peak at $T_m \sim$ 300 K and a broad shoulder at a lower temperature $T_s \sim$ 270 K. These two anomalies can be correlated to temperature dependent transition to a tetragonal polar phase and further increase in tetragonality in the polar phase, respectively, which are characterized from synchrotron X-ray diffraction. The pyroelectric coefficient ($\partial P/\partial T$) and electrocaloric

properties for this material are furthermore examined. Interestingly, the material exhibits two peaks for temperature dependence of pyroelectric coefficient with values of $-(\partial P/\partial T) \sim 563$ $\mu C/(m^2 K)$ at $T \sim 270$ K and $-(\partial P/\partial T) \sim 1021$ $\mu C/(m^2 K)$ at $T \sim 320$ K, which correlates to the temperature-dependent structural changes. In addition, a broad peak for electrocaloric temperature change near 320 K is predicted from Maxwell relations, which gives rise to a high relative cooling power of ~ 17 J/kg. The study shows that length scale–specific structural changes can be induced at different temperature ranges in this material, which can be selectively used for pyroelectric energy harvesting or electrocaloric cooling.

Results and discussion

Dielectric properties

The real part of dielectric permittivity (ε') and dissipation factor (tan δ) of the BCST-Nb$_{0.04}$ samples were measured in the frequency (f) range of 100 Hz $\leq f \leq$ 100 kHz and for temperature (T) range of 173–373 K. The results are shown in Fig. 2(a). The ε' versus T curve exhibits a main peak at $T_m \sim$ 300 K, whereas an additional shoulder (T_s) is noticed between 225 and 270 K. We also observe that T_m shifts up by 2.5 K, and the maximum permittivity at $\sim T_m$ decreases in magnitude,
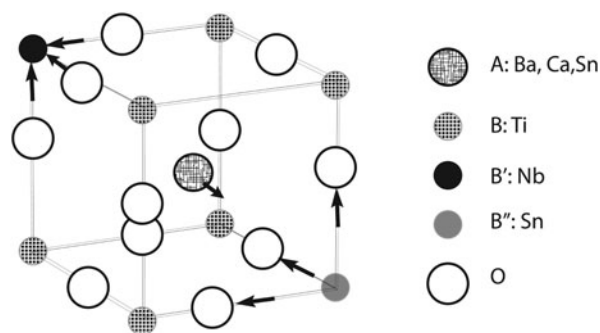
when the frequency is increased from 0.1 to 100 kHz. This behavior provides evidence of the relaxor-like behavior for the BCST-Nb$_{0.04}$ ceramics [13, 25, 26, 27].

In the case of normal ferroelectrics, the temperature-dependent dielectric permittivity follows the Curie–Weiss law; $1/\varepsilon' = (T - T_C)/C$, where C is the Curie constant and T_C is the Curie–Weiss temperature [28]. By contrast, the relaxation of the electric dipoles can lead to significant deviation from Curie–Weiss law above T_m [29]. In such cases, ε' (T) can be modeled following the Uchino and Nomura formula, also known as the modified Curie–Weiss law [30].

$$\left(\frac{1}{\varepsilon'} - \frac{1}{\varepsilon_m}\right) = \frac{(T - T_m)^\gamma}{C} \quad , \qquad (1)$$

where ε_m is the maximum of ε' at T_m, and the coefficient γ represents the degree of diffuseness for the transition across T_m. γ is equal to 1 for normal ferroelectric behavior, and it varies between 1 and 2 for relaxor ferroelectrics [30]. Accordingly, the γ value has been evaluated from the slope of the $\log(1/\varepsilon' - 1/\varepsilon'_m)$ versus $\log(T - T_m)$ graph, (see Supplementary material Fig. S1). The obtained value of γ for the BCST-Nb$_{0.04}$ ceramics is 1.89 $\pm$ 0.01 (f = 1 kHz) (γ is close to 2 at higher frequencies), which is comparable to that of other Pb-free ferroelectric relaxors listed in Table I [29, 31, 32, 33, 34, 35]. The critical exponent γ depends on the underlying ordering mechanism; $\gamma \sim 1$ for pure Curie–Weiss behavior or mean field theory, $\gamma \sim 1.3$ for 3D random bond Ising model, whereas γ is higher for random field Ising models and approaches values close to 2 [36, 37, 38]. The relatively high values of γ for the current material and others listed in Table I might be related to the strong random field interactions in these materials, although it needs to be carefully evaluated with high-precision dielectric measurements over broader frequency ranges.

To further examine the relaxor behavior in this material, we analyze the frequency dispersive dielectric permittivity using Arrhenius model and Vogel–Fulcher model [39, 40]. The unphysical parameters obtained from the fitting analysis

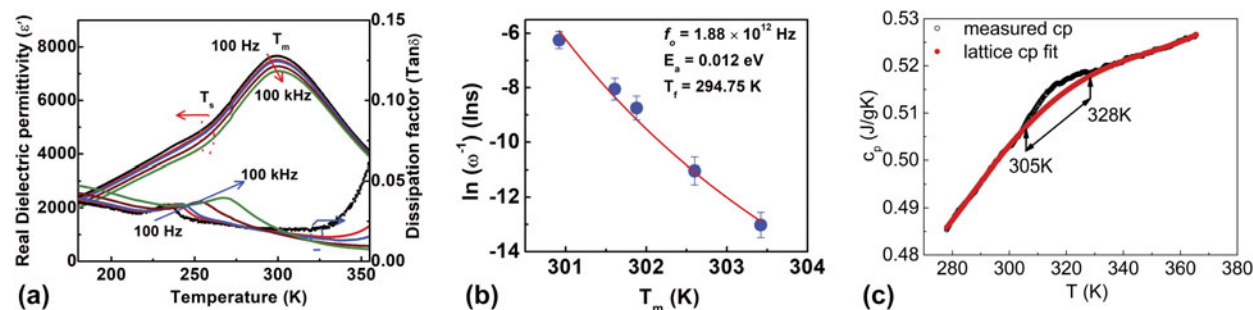**Figure 1:** Proposed substitution scheme for BaTiO$_3$ to induce multisite atomic displacements.

Figure 2: (a) Temperature-dependent real part of dielectric permittivity $\varepsilon'(T)$ and dissipation factor (tan δ) of BCST-Nb$_{0.04}$ ceramics measured at various frequencies (100 Hz $\leq f \leq$ 100 kHz). (b) The logarithmic inverse frequency variation of transition temperature T_m (shown by round symbols) and the corresponding solid continuous line is the best fit to the Vogel–Fulcher law. (c) Specific heat measurement shows a broad hump in the temperature range of 305–328 K. Such broad phase transition is typically observed for ferroelectrics which deviate from Curie–Weiss law.

TABLE I: Comparison of various parameters of Pb-free perovskite relaxor ferroelectrics along with results from the present study.

Material	E_a (eV)	T_f (K)	f_o (Hz)	γ	Reference
$Ba(Ti_{0.7}Hf_{0.3})O_3$	0.14	78.5	1.53×10^{13}	1.87	[28]
$Ba(Ti_{1-y}Ce_y)O_3$ ($y = 0.06$)	3.9	374.1	1.44×10^{11}	2	[29]
$0.8K_{0.5}Na_{0.5}NbO_3-0.2Ba_{0.5}Sr_{0.5}TiO_3$	0.0113	305	6.95×10^{9}	1.70	[30]
$0.95BaTiO_3-0.05Bi(Zn_{2/3}Nb_{1/3})O_3$	0.029	247	5.04×10^{9}	1.53	[25]
$Ba(Zr_{0.25}Ti_{0.75})O_3$	0.15	128	1.03×10^{11}	1.71	[31]
$BCST-Nb_{0.04}$	0.0128	294.75	1.875×10^{12}	1.88	This study

using Arrhenius model (shown in Supplementary material Fig. S2) indicate that dipole dynamics appear only above the freezing temperature (T_f). The concept of T_f, which is similar to spin or dipolar glass, is incorporated in the Vogel–Fulcher model and can be expressed as [41]

$$\omega = \omega_o \exp\left[\frac{-E_a}{k_B(T_m - T_f)}\right] \quad , \qquad (2)$$

where $\omega = 2\pi f$ ($f =$ is the measured frequency), $\omega_o = 2\pi f_o$, ($f_o =$ is the attempt jump frequency), E_a is the activation energy, and k_B are the Boltzman constant. Figure 2(b) shows fitting of the dielectric permittivity data using Vogel–Fulcher model. From the analysis, we obtained $E_a = 0.012 \pm 0.001$ eV, $f_o = 1.88 \times 10^{12}$ Hz, and $T_f = 294.75 \pm 2$ K. Corresponding values for other relaxor ferroelectrics are also listed in Table I. The attempt jump frequency obtained in the present case are similar those observed for relaxor ferroelectrics, which lies between 10^9 Hz and 10^{14} Hz [13, 39, 40, 41]. The value of E_a of $BCST-Nb_{0.04}$ is quite low compared with other Pb-free relaxor materials, e.g., $0.95BaTiO_3-0.05Bi(Zn_{2/3}Nb_{1/3})O_3$ [29] and $0.8K_{0.5}Na_{0.5}NbO_3-0.2Ba_{0.5}Sr_{0.5}TiO_3$ [34], and signifies easier reorientation of local dipoles in the $BCST-Nb_{0.04}$ ceramics.

The microscopic phase below T_m can be furthermore ascertained from specific heat measurements. For transition below T_m from polar nano regions (PNR) to a ferroelectric state with nanoscale domains, one can expect heat capacity C_p in excess of what is predicted from classical thermodynamic laws [42, 43]. By contrast, if no excess heat capacity is observed near T_m, the nanoscale ferroelectric model can be dismissed in favor of a transition to a dipolar glass state. For the present system, a broad anomaly in the form of excess C_p is observed in the range of 305–328 K [Fig. 2(c)], which indicates transition from PNRs at higher temperatures to ferroelectric domains below T_m. Nevertheless, the rather weak and broad nature of the peak for excess specific heat point to the lack of establishment of a true long-range order [44]. Piezoresponse force microscopy corroborates the findings above as only nanoscale domains can be observed at RT (see Fig. S3 in Supplementary material).

Analysis of average and local atomic structures

The structural transitions accompanying the different anomalies observed in the dielectric spectrum are analyzed using X-ray diffraction and total scattering data, as presented below.

Average atomic structure

The average atomic structure was modeled from the X-ray diffraction patterns in the temperature range of 220 K $\leq T \leq$ 380 K using Rietveld refinement implemented in the FULL-PROF suite software [45]. First, to determine if Sn disproportionate into Sn^{2+} and Sn^{4+} oxidation states, we performed the X-ray photoelectron spectroscopy (XPS) measurements. The XPS spectra of $BCST-Nb_{0.04}$ along with the pure SnO (Sn^{2+}) and SnO_2 (Sn^{4+}) are shown in the Supplementary material Fig. S4. Two peaks are observed for Sn in $BCST-Nb_{0.04}$ ceramics, indicated as $Sn-^3d_{5/2}$ and $^3d_{3/2}$. A high energy tail is present on the $^3d_{3/2}$ peak, indicating that both oxidation states are present in the compound. Both peaks are deconvoluted into two peaks centered at 485.48 eV (P_1) and 485.68 eV (P_2), and 493.93 eV (P_3) and 495.15 eV (P_4), respectively. Peaks P_1 and P_3 correspond to Sn^{2+}, and peaks P_2 and P_4 correspond to Sn^{4+}. All of these closely match the reference energies obtained from SnO and SnO_2 [46, 47]. From peak fitting analysis of XPS data, we estimate close to equal concentration of Sn^{2+} and Sn^{4+} ($Sn^{2+}:Sn^{4+} = 0.57:0.43$). These values are therefore used as initial parameters for concentration of Sn^{2+} and Sn^{4+} in Rietveld models.

Figure 3(a) shows a representative fit for the diffraction pattern measured at 300 K. The peaks were fit using a Pseudo-Voigt profile. The background was fitted with a Chebychev polynomial. The scale factor, zero-point correction, isotropic thermal parameters, lattice parameters, and positional coordinates were refined. It was observed that from 220 to 360 K, the best fit was achieved for a tetragonal phase with $P4mm$ space group, whereas for 380 K, the best fit was achieved for a cubic phase with the $Pm\bar{3}m$ space group. All the structural parameters obtained from the final Rietveld refinement analysis are listed in Table II. Figure 3(b) shows "tetragonality" or "c/a" ratio of the structure as a function of temperature. The c/a ratio increases with decreasing temperature. However, the increase in not linear and a sharper increase is observed below $T \sim 270$ K. The nonlinear deviation in the c/a ratio of the average structure below 270 K is most likely due to an increase in the medium–range correlations arising as a result of growth of polar nanodomains. The onset of nonlinear increase in tetragonality coincides with T_s in Fig. 2(a).

Above 320 K, we use dotted line to show the variation in c/a ratio because no diffraction data were measured in the intervening temperatures. Nevertheless, the temperature-
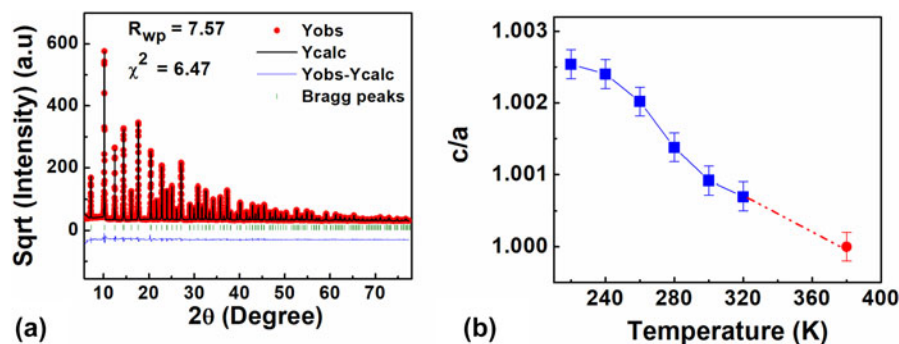
Figure 3: (a) The measured X-ray diffraction pattern of BCST-Nb$_{0.04}$ ceramics at RT along with the calculated pattern from Rietveld refinement. (b) The temperature-dependent change in tetragonality (c/a) of the unit cell. The dotted line in between 320 and 380 K indicates that no diffraction data were collected in this temperature range, and therefore no claim for structural changes in this range is made.

TABLE II: List of structural parameters obtained from Rietveld refinement of Ba$_{0.77}$Ca$_{0.21}$Sn$_{0.02}$(Ti$_{0.94}$Nb$_{0.04}$Sn$_{0.02}$)O$_3$.

T	220 K	240 K	260 K	280 K	300 K	320 K	380 K
Space group	$P4mm$	$P4mm$	$P4mm$	$P4mm$	$P4mm$	$P4mm$	$Pm\bar{3}m$
R_{wp}	6.7	6.85	7.07	7.57	8.34	8.17	8.28
Chi [2]	5.14	5.39	5.70	6.47	7.83	7.51	7.63
$a = b$ (Å)	3.982 (13)	3.983 (2)	3.984 (2)	3.985 (3)	3.986 (4)	3.987 (6)	3.989 (7)
c (Å)	3.992 (2)	3.992 (4)	3.992 (4)	3.990 (6)	3.990 (4)	3.989 (12)	3.989 (7)
V (Å^3)	63.338 (5)	63.354 (7)	63.370 (8)	63.386 (11)	36.422 (7)	63.425 (2)	63.501 (19)
$Z_{A\ atom}$	0.0001	0.0001	0.0001	0.0001	0.0001	0.0001	0
$Z_{B\ atom}$	0.505 (17)	0.502 (2)	0.502 (2)	0.500 (2)	0.501 (3)	0.496 (4)	0.5
Z_{O_1}	−0.007 (7)	−0.008 (7)	−0.013 (5)	−0.017 (4)	−0.016 (6)	0.013 (11)	0
Z_{O_2}	0.472 (18)	0.475 (2)	0.474 (2)	0.473 (3)	0.474 (4)	0.522 (6)	0.5
U_{iso} Ba (Å^2)	0.00280 (5)	0.00307 (6)	0.0032 (6)	0.00343 (5)	0.0037 (8)	0.0041 (7)	0.0037 (4)
U_{iso} Ti (Å^2)	0.0025 (14)	0.0029 (14)	0.0031 (14)	0.0033 (9)	0.0034 (10)	0.003 (18)	0.0037 (9)
U_{iso} O$_1$ (Å^2)	0.0017 (13)	0.0013 (14)	0.0002 (14)	0.0012 (6)	0.0001 (2)	0.0042 (2)	0.004 (7)
U_{iso} O$_2$ (Å^2)	0.0055 (9)	0.0065 (9)	0.0065 (10)	0.0069 (13)	0.0064 (17)	0.006 (19)	0.008 (4)

dependent C_P measurement [Fig. 2(c)] shows an anomaly beginning at 328 K, which closely corresponds to the starting temperature for transition from cubic to tetragonal structure.

Local structure analysis from X-ray total scattering

The temperature-dependent evolution of the local atomic structure within the polar nanodomains are analyzed using the X-ray pair distribution function (PDF) method [48]. Figure 4(a) shows the PDFs in the region $1.5 < r < 9.5$ Å (full range shown in Fig. S5), in the temperature range of 80–400 K. Each of the different bond lengths contained within a single unit cell is labeled. The bond between the A-site and the 2nd nearest B-site atoms is also included because of its close proximity to the M–M$_3$ bond. The peaks between $8.3 < r < 9.5$ Å correspond to contributions from all possible ionic pairs and relate to the medium range order [49].

At 80 K, each peak is well defined, and small peaks corresponding to split in A–O bond lengths are visible. A split in the A–O PDF peak demonstrates that substitution of Ca^{2+} and Sn^{2+} at the A site breaks the degeneracy of the A–O bond distances. At higher temperatures, the thermal motion increases,

causing this detail to "smooth" out. Rietveld-type fits of the whole PDF data across the region $1.0 < r < 60.0$ Å were carried out using the software TOPAS [50]. Representative fits are shown in Fig. 4(b) at 300 K for models of orthorhombic ($Amm2$), tetragonal ($P4mm$), and cubic ($Pm\bar{3}m$) symmetries [51]. The residuals show that the orthorhombic structure produces the best fit. This indicates that although the long-range average structure (from Rietveld refinement of X-ray diffraction data) shows tetragonal symmetry, the local structure appears to have orthorhombic distortions. Similar behavior was also reported earlier by Laurita et al. for inclusion of Sn^{2+} at the A site, even at very small concentrations [21].

To further assess the length scales of the distortions, present in the structure, orthorhombic box car refinements were performed, and the results are shown in Fig. 4(c). Here, fitting boxes with r-ranges of 6.5 Å starting from 1 Å and overlapped by 0.5 Å were used. To have a clear comparison with the pseudotetragonal perovskite structure, the monoclinic equivalent lattice parameters were calculated for the ortho-rhombic unit cell [52]. Interestingly, the short-range lattice parameters are smaller than the long-range average, which then tends toward average values with the increase in r. An
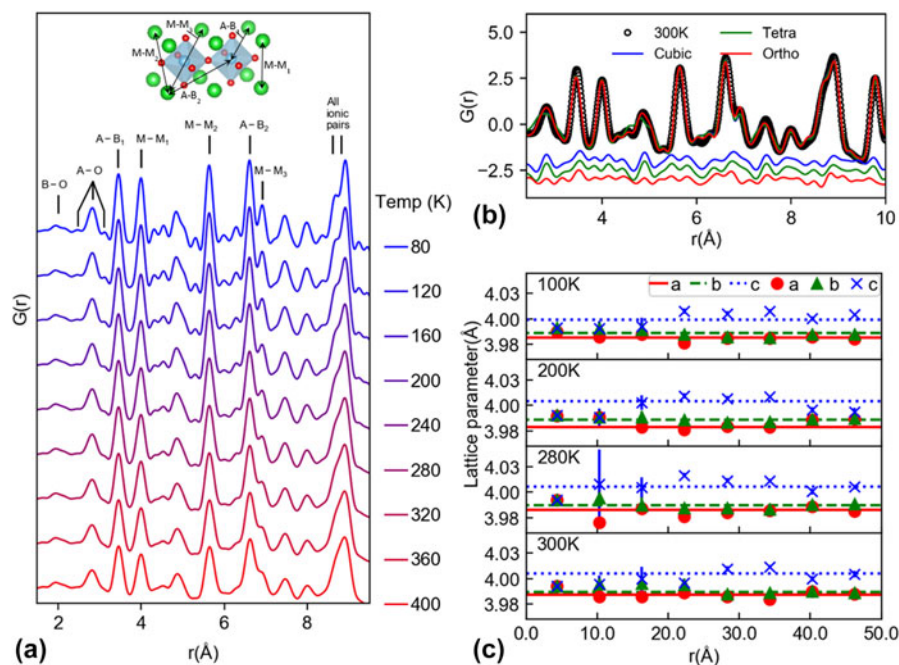
Figure 4: X-ray PDF results for BCST-Nb$_{0.04}$ (a) The temperature evolution of the PDF over the local-scale structural region with 2 unit-cell inset illustrating bonds between A and B sites (A–B) and bonds between equivalent A–A or B–B sites, labeled as M–M. The subscript numbers refer to the shortest–longest bond lengths, respectively. (b) Rietveld PDF refinement results at 300 K, with orthorhombic, tetragonal, and cubic fits overlaid on the raw data and difference plots below. (c) Pseudocubic equivalent lattice parameters from whole and box-car orthorhombic PDF refinements at 100, 200, 280, and 300 K. Markers correspond to the box-car refinements and are plotted with respect to the center of the box r-range, whereas the horizontal lines correspond to the lattice parameters from fitting the whole PDF. Vertical lines on the markers correspond to the error bars.

explanation could be that the A- and B-site atoms have both positive and negative local correlations that result in the nearest-neighbor A–B and M–M peaks to display an overall cubic local structure, see Fig. 4(a). This indicates that the short-range atomic correlations in this material are significantly more complicated than an orthorhombic model, which is rather unusual compared with other box-car studies based on relaxors [53] and warrants further investigation via other techniques, e.g., neutron PDF, and EXAFS or big box modeling.

Hysteresis loops and electrothermal properties

Relaxor ferroelectrics exhibit attractive electrothermal properties, viz. pyroelectric and electrocaloric effects. The pyroelectric effect is defined as a change in spontaneous polarization as function of temperature. The resultant short-circuit pyroelectric current i_p is given by

$$i_p = A \left(\frac{\partial P}{\partial T} \right) \left(\frac{dT}{dt} \right) \quad , \tag{3}$$

where A is a constant, $\partial P / \partial T$ is the pyroelectric coefficient $P(T)$ and dT/dt is the temporal rate of change in temperature. In recent years, pyroelectric effect has received much attention for potential application to recover electrical energy from waste heat [5]. The converse of pyroelectric effect is the electrocaloric effect or reversible change in temperature as a function of

applied electric field. It is well known that the electrocaloric effect and pyroelectricity are related by the Maxwell relation in thermodynamics, and it can be expressed as:

$$\left(\frac{\partial P}{\partial T} \right)_E = \left(\frac{\partial S}{\partial E} \right)_T \quad , \tag{4}$$

where S is the entropy, E is the applied electric field, and P is the total macroscopic polarization. Using the above relation, we can calculate the adiabatic temperature change ΔT and isothermal entropy change ΔS from the following equations:

$$\Delta T = -\frac{1}{C_p \rho} \int_{E_1}^{E_2} T \left(\frac{\partial P}{\partial T} \right)_E dE \quad , \tag{5}$$

$$\Delta S = -\frac{1}{\rho} \int_{E_1}^{E_2} \left(\frac{\partial P}{\partial T} \right)_E dE \quad , \tag{6}$$

where P is the polarization, ρ is the mass density, T is the absolute temperature, E_1 and E_2 are the starting and final values of the electric fields, respectively, and C_p is the heat capacity [54]. It can be seen that a large $(\partial P / \partial T)$ over a broad temperature range is desirable for both pyroelectric energy recovery as well as electrocaloric applications. In this regard, the attractiveness of relaxor ferroelectrics becomes clear, as they exhibit a broad permittivity peak and relatively large slope of $(\partial P / \partial T)$ over a broad temperature range.
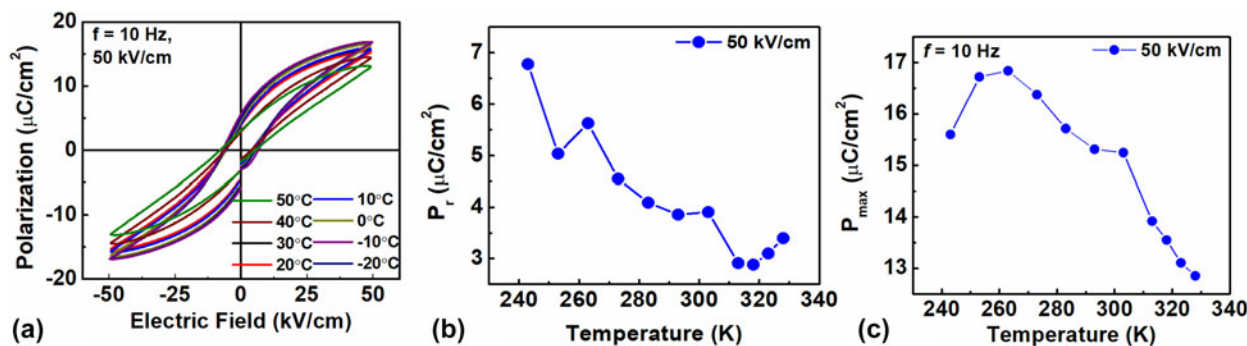
Figure 5: (a) *P–E* loops of BCST-Nb$_{0.04}$ ceramics measured at selected temperatures for applied electric fields of frequency 10 Hz. (b, c) temperature-dependent changes in remanent polarization (P_r) (b), and maximum polarization (P_{max}) (c), which are obtained from the *P–E* loops.
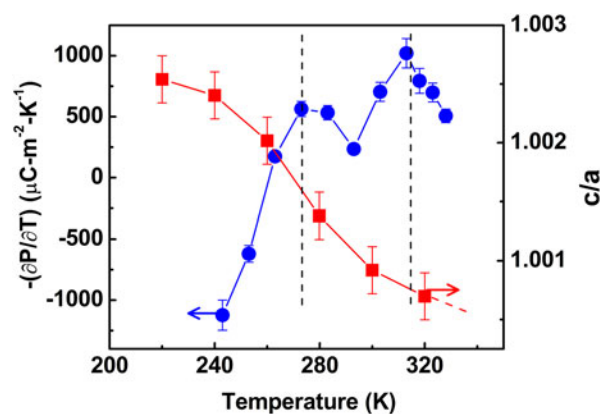

Figure 6: (L.H.S) Pyroelectric coefficient, i.e., $-(\partial P/\partial T)$ as a function of temperature. (R.H.S.) Change in tetragonality "*c/a*" as a function of temperature.

To characterize the electrothermal properties of BCST-Nb$_{0.04}$ ceramics, the polarization versus electric field (*P–E*) loops were recorded under ac fields of frequency 10 Hz and field amplitude of 50 kV [Fig. 5(a)]. To avoid electrothermal history, after measuring the *P–E* loop at each temperature, the sample was again heated to the paraelectric state (>50 °C) and then cooled down to the next desired measuring temperature. The remnant polarization (P_{max}) and maximum polarization (P_r) were extracted from the *P–E* loops. The results are shown in Figs. 5(b) and 5(c), respectively. Several interesting features can be noted from the temperature-dependent P_{max} (*T*) and P_r (*T*) curves. P_{max} first increases and then decreases with increasing temperature, with the inflection point located at $T_s \sim 270$ K. The P_r (*T*) continuously decreases with increasing temperature up to 320 K except for a deviation at $T_s \sim 270$ K. A small increase in P_r appears above 320 K, which is an experimental artifact due to increase in leakage current. Above T_m, decaying trends for both P_{max} and P_r are observed, which indicates deviation from long-range ordered ferroelectric state [55].

The pyroelectric coefficient ($\partial P/\partial T$) calculated from the P_{max} (*T*) curve is shown in Fig. 6. A broad peak for pyroelectric coefficient near $T_s \sim 270$ K with $-(\partial P/\partial T) \sim 563$ μC/(m^2 K)

essentially results from an inflection in the P_{max} versus *T* curve at this temperature. We note that this also correlates with nonlinear increase in c/a ratio near $T_s \sim 270$ K, which is likely due to transition to longer range domains. Similar equivalence between temperature-dependent and field-dependent transitions to longer range correlations was noted earlier for the prototypical relaxor PMN [45]. Therefore, we propose that the broad peak for ΔT at 270 K is likely due to enhanced susceptibility for electric field–induced growth of polar nanodomains. We observed a second peak for pyroelectric coefficient at $T_m \sim 320$ K with $-(\partial P/\partial T)_E \sim 1021$ μC/(m^2 K). The second peak can be correlated to the excess C_p observed at ~ 320 K, where the system transforms from a cubic to a tetragonal structure as evident from analysis of the average crystallographic structure.

The two broad peaks for pyroelectric coefficient observed in the range of 270–325 K can be potentially useful for energy harvesting by utilizing the induced pyroelectric current from large thermal fluctuations, as indicated by Eq. (3). A useful figure of merit (FOM) for pyroelectric energy harvesting is given by [55]

$$F_E = \frac{(\partial P/\partial T)^2}{\varepsilon} \quad . \tag{7}$$

Using Eq. (7), we obtain $F_E \sim 6.5$ J/(m^3 K^2) for the peak at $T \sim 270$ K and $F_E \sim 17.5$ J/(m^3 K^2) for the peak at $T \sim 320$ K, which are comparable to the values for Pb-based ferroelectric materials [55].

The electrocaloric temperature change (ΔT) and isothermal entropy change (ΔS) for BCST-Nb$_{0.04}$ ceramics are calculated using Eqs. (5) and (6) and using data shown in Fig. 6. The values for ΔT and ΔS obtained using Maxwell equations are shown in Figs. 7(a) and 7(b). A peak value of $\Delta T \sim 0.6$ K is predicted at 320 K from Maxwell relations, which is comparable to several Pb-based and Pb-free relaxors [56, 57, 58, 59]. Furthermore, direct measurements of electrocaloric temperature changes were also obtained for comparison with those
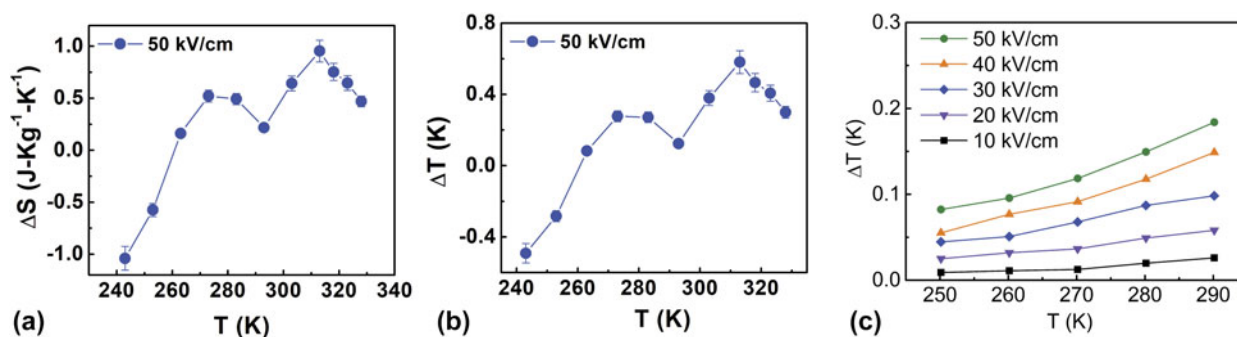
Figure 7: (a) Entropy change (ΔS) under applied electric field as a function of temperature for BCST-Nb$_{0.04}$ ceramics. (b) Corresponding electrocaloric temperature changes (ΔT) as function of temperature. Results shown in (a, b) are obtained from P–E loops by application of Maxwell relations. (c) ΔT measured directly as a function of temperature.

calculated using Eq. (5), which are shown in Fig. 7(c). The values of ΔT obtained from direct measurements are slightly smaller than those obtained from indirect measurements, which could be related to limitations in reaching equilibrium conditions as necessary for application of Maxwell relations. For temperatures above 300 K, it was not possible to reliably determine ΔT from direct measurements due to Joule heating.

One interesting aspect to note is that application of Maxwell relations below 270 K results in a negative ΔT. Nevertheless, no negative electrocaloric temperature change was observed in direct measurements. Similar discrepancies between direct and indirect measurements were noted earlier, such as Refs. 56 and 60. In most cases, this discrepancy originates from peculiar polarization behavior (related to change in domain structure), which results in a different $P(T)$ relations. In the present case, the negative ΔT below 270 K could be related to the growth of the polar nanodomain structure below this temperature, which is indicated from X-ray structural analysis as presented in section "Analysis of average and local atomic structures".

A broader temperature range for large $(\partial P/\partial T)$ is desirable for cooling applications. Classical ferroelectrics with sharp first-order transitions typically result in a higher electrocaloric temperature change due to higher contribution from latent heat, although the temperature span of high properties is typically limited only to about 10 K [61, 62]. On the other hand, in relaxor ferroelectrics, the temperature span of higher electrocaloric properties is wider (30 K or more) [61, 63, 65]. This is because of the ergodic temperature range of relaxors, where transition between relaxor and ferroelectric phase is reversible. However, the ECE temperature change in relaxor system is typically smaller than that in ferroelectrics because of smaller latent heat contribution when the ferroelectric phase is induced. Therefore, for a fair comparison of usefulness of electrocaloric materials for refrigeration applications, it is imperative to calculate the relative cooling power or refrigeration capacity (RC), which is given by the following equation:

$$\mathrm{RC} = \int_{T_1}^{T_2} \Delta S(T) \mathrm{d}T \quad . \tag{8}$$

To calculate RC, we integrated the area under the $\Delta S(T)$ peak at $T \sim 320$ K [Fig. 7(a)] over full-width at half-maxima (FWHM) ($T_1 = 303.8$ K and $T_2 = 321.6$ K). A value of RC $\sim$ 17 J/kg is obtained for the current material using Eq. (8), which is higher than the value of RC $\sim$ 11.87 J/kg reported for Pb-based relaxors [59].

Conclusion

A new Pb-free relaxor system was obtained by adopting a combined A- and B-site substitution scheme in the prototypical ferroelectric BaTiO$_3$. The dielectric spectrum of this material shows a peak permittivity at $T_m \sim 298$ K ($f = 1$ kHz) along with a broad shoulder at $T_s \sim 270$ K. The frequency dispersive behavior in the $\varepsilon'(T)$ follows the Uchino and Nomura and Vogel–Fulcher relations, which further informs about the relaxor ferroelectric behavior. Existence of an anomaly in the temperature dependence of C_p, as well as Rietveld analysis of high-resolution X-ray diffraction data, indicates that below T_m, the material transforms from a cubic to an average tetragonal phase. Analysis of local structure from X-Ray PDF shows that in short-range scale <9 Å, the local structure is close to orthorhombic and remains unchanged in the temperature range 100–300 K. In addition, a strong non-linear deviation in the temperature dependence of the c/a ratio of the average tetragonal phase is observed below $T_s \sim 270$ K, which is likely associated with an increase in the size of polar nanodomains. The temperature-dependent structural transitions can be correlated to the electrothermal properties of the material. Based on temperature-dependent polarization measurements, we observed two peaks in the $(\partial P/\partial T)$ curve in the temperature range of 250–320 K: (i) -$(\partial P/\partial T) \sim 563$ μC/(m^2 K) at $T \sim 270$ K, and (ii) -$(\partial P/\partial T) \sim 1021$ μC/(m^2 K) at $T \sim 320$ K.

In addition, the broad peak in $(\partial P/\partial T)$ near $T \sim 320$ K gives rise to a large electrocaloric temperature change with relative cooling power of ~ 17 J/kg. These properties make BCST-$Nb_{0.04}$, a potential candidate for pyroelectric energy harvesting and electrocaloric cooling over broad temperature range.

Methods

Material synthesis

Polycrystalline $Ba_{0.77}Ca_{0.21}Sn_{0.02}(Ti_{0.94}Nb_{0.04}Sn_{0.02})O_3$ (BCST-$Nb_{0.04}$) ceramics were prepared using solid-state synthesis from high-purity $BaCO_3$ (99.5%), $CaCO_3$ (99%), SnO_2 (99.8%), TiO_2 (99%), and Nb_2O_5 (99.9%) as precursors. Appropriate amounts of all these raw materials were weighed and mixed thoroughly for 24 h using zirconia balls in a plastic jar. The balls to powder weight ratio was maintained at 5:1. Ethanol was used as a milling medium. The mixed powder slurry was then dried at 100 °C for 12 h in an oven. The dried powder mixture was calcined at 1350 °C for 6 h in a box furnace. After that, the calcined powder was ground, sieved, and pressed into 10-mm diameter pellets by applying a uniaxial pressure ~ 140 MPa. Finally, all the pellets were sintered at ~ 1450 °C for 4 h in air to obtain the desired ceramics. The relative density of the final sintered samples was found to be $\sim 92.8\%$ by Archimedes method.

Electrical and electrothermal measurements

The temperature-dependent (173 K $\leq T \leq$ 373 K) as well as frequency-dependent (100 Hz $\leq f \leq$ 100 kHz) dielectric properties were measured using a LCR meter (Agilent-4284A) connected to a heating and cooling ($\sim$liquid nitrogen temperature) setup. A Radiant Precision LC-II Ferroelectric Test System was used to measure the electric-field-dependent polarization (P–E loops) at various temperatures using applied fields of frequency 10 Hz.

The heat capacity measurements (C_p) were performed in a computerized homemade ac-calorimeter. A detailed description of the ac operation mode can be found elsewhere [64]. The electrocaloric temperature change was measured in a homebuilt measurement chamber with a stable surrounding temperature of ± 2 mK. The temperature change of the sample was recorded by a small bead thermistor (NTC GLS9, TE Connectivity Measurement Specialists Ltd.) attached to the sample surface.

Structural characterization

The structural characterization of all the samples were performed at various temperatures (220 K $\leq T \leq$ 380 K) using Rietveld refinement of X-ray diffraction and X-ray PDF analysis. High-resolution diffraction patterns were measured at the SPring-8 using X-ray radiation of wavelength $\lambda =$ 0.49988 Å. X-ray total scattering patterns were measured at the Sector 11-ID-B of the Advanced Photon Source using X-rays of energy $E = 86.72$ keV and wavelength $\lambda = 0.143$ Å. The sample to detector distance was kept at 251.1 mm. The maximum scattering vector (Q_{max}) was limited to 29 Å^{-1}. The PDF patterns were obtained from the X-ray total scattering patterns using PDFgetX2 [65]. Quantitative elemental composition of all the samples was analyzed by means of XPS with Physical electronics (PHI 5802) system using Al-K_α source (1486.6 eV). The XPS data were collected in the range of 0–1200 eV.

Author contributions

The manuscript was written through contributions of all authors. All authors have given approval to the final version of the manuscript.

Funding sources

Acknowledgments

Supplementary material

To view supplementary material for this article, please visit https://doi.org/10.1557/jmr.2020.25.

References

1. **L.E. Cross**: Relaxor ferroelectrics. *Ferroelectrics* **76**, 241–267 (1987).

2. **G.A. Smolenskii, V.A. Isupov, A.I. Agranovskaya, S.N. Popov**: Ferroelectrics with diffuse phase transitions. *Sov. Phys. Solid State* 2: 2584–94 (1961).

3. **K. Uchino**: *Piezoelectric Actuators and Ultrasonic Motors* (Kluwer Academic, Boston, 1996).

4. **Z. Kutnjak, J. Petzelt, and R. Blinc**: The giant electromechanical response in ferroelectric relaxors as a critical phenomenon. *Nature* **441**, 956–959 (2006).

5. **S.P. Alpay, J. Mantese, S. Trolier-McKinstry, Q. Zhang, and R.W. Whatmore**: Next-generation electrocaloric and pyroelectric materials for solid-state electrothermal energy interconversion. *MRS Bull.* **39**, 1099–1109 (2014).

6. **G.A. Samara**: The relaxational properties of compositionally disordered ABO_3 perovskites. *J. Phys.: Condens. Matter* **15**, R367–411 (2003).

7. **A.A. Bokov and Z-G. Ye**: Recent progress in relaxor ferroelectrics with perovskite structure. *J. Mater. Sci.* **41**, 31–52 (2006).

8. **W. Kleemann**: The relaxor enigma—Charge disorder and random fields in ferroelectrics. *J. Mater. Sci.* **41**, 129–136 (2006).

9. **D. Fu, H. Taniguchi, M. Itoh, S-Y. Koshihara, N. Yamamoto, and S. Mori**: Relaxor $Pb(Mg_{1/3}Nb_{2/3})O_3$: A ferroelectric with multiple inhomogeneities. *Phys. Rev. Lett.* **103**, 207601-1-4 (2009).

10. **W. Dmowski, S.B. Vakhrushev, I-K. Jeong, M.P. Hehlen, F. Trouw, and T. Egami**: Local lattice dynamics and the origin of the relaxor ferroelectric behavior. *Phys. Rev. Lett.* **100**, 137602–137605 (2008).

11. **K. Binder and A.P. Young**: Spin glasses: Experimental facts, theoretical concepts, and open questions. *Rev. Mod. Phys.* **58**, 801–974 (1986); K. H. Fischer and J. A. Hertz: *Spin Glasses* (Cambridge University Press, Cambridge, 1991).

12. **C.A. Angell**: Perspective on the glass transition. *J. Phys. Chem. Solids* **49**, 863–871 (1988).

13. **R.A. Cowley, S.N. Gvasaliya, S.G. Lushnikov, B. Roessli, and G.M. Rotaru**: Relaxing with relaxors: A review of relaxor ferroelectrics. *Adv. Phys.* **60**, 229–327 (2011).

14. **V.V. Shvartsman and D.C. Lupascu**: Lead-free relaxor ferroelectrics. *J. Am. Ceram. Soc.* **95**, 1–26 (2012).

15. **I-W. Chen, P. Li, and Y. Wang**: Structural origins of relaxor perovskites. *J. Phys. Chem. Solids* **57**, 1525–1536 (1996).

16. **P.K. Davies and M.A. Akbas**: Chemical order in PMN-related relaxors: Structure, stability, modification and impact on properties. *J. Phys. Chem. Solids* **61**, 159–166 (2000).

17. **R.E. Cohen**: Origin of ferroelectricity in perovskite oxides. *Nature* **358**, 136–138 (1992).

18. **R.E. Cohen and H. Krakauer**: Lattice dynamics and origin of ferroelectricity in $BaTiO_3$: Linearized-augmented-plane-wave total-energy calculations. *Phys. Rev. B* **42**, 6417–6423 (1990).

19. **D. Fu, M. Itoh, S-Y. Koshihara, T. Kosugi, and S. Tsuneyuki**: Anomalous phase diagram of ferroelectric $(Ba,Ca)TiO_3$ single crystals with giant electromechanical response. *Phys. Rev. Lett.* **100**, 227601–227604 (2008).

20. **S. Suzuki, T. Takeda, A. Ando, and H. Tkagi**: Ferroelectric phase transition in Sn^{2+} ions doped $(Ba,Ca)TiO_3$ ceramics. *Appl. Phys. Lett.* **96**, 132903–132906 (2010).

21. **G. Laurita, K. Page, S. Suzuki, and R. Sehadri**: Average and local structure of the Pb-free ferroelectric perovskites $(Sr,Sn)TiO_3$ and $(Ba,Ca)TiO_3$. *Phys. Rev. B* **92**, 214109–214118 (2015).

22. **M.S. Moreno, G. Punte, G. Rigotti, R.C. Mercader, A.D. Weisz, and M.A. Blesa**: Kinetic study of the disproportion of tin monoxide. *Solid State Ionics* **144**, 81–86 (2001).

23. **M. Kwoka, L. Ottaviano, M. Passacantando, S. Santucci, G. Czempik, and J. Szuber**: XPS study of the surface chemistry of L-CVD SnO_2 thin films after oxidation. *Thin Solid Films* **490**, 36–42 (2005).

24. **S. Suzuki, T. Takeda, A. Ando, T. Oyama, T. Wada, H. Niimi, and H. Takagi**: Effect of Sn^{2+} ion substitution on dielectric properties of $(Ba,Ca)TiO_3$ ferroelectric ceramics. *Jpn. J. Appl. Phys.* **49**, 09MC04-1-5 (2010).

25. **G. Shirane, J.D. Axe, J. Harada, and J.P. Remeika**: Soft ferroelectric modes in lead titanate. *Phys. Rev. B* **2**, 155–159 (1970).

26. **R.A. Cowley**: The phase transition of strontium titanate. *Philos. Trans. R. Soc. London* **354**, 2799 (1996).

27. **K. Kakimoto, I. Masuda, and H. Oshato**: Ferroelectric and piezoelectric properties of $KNbO_3$ ceramics containing small amounts of $LaFeO_3$. *Jpn. J. Appl. Phys.* **42**, 6102–6105 (2003).

28. **G.H. Jonker**: On the dielectric curie-weiss law and diffuse phase transition in ferroelectrics. *Mater. Res. Bull.* **18**, 301–308 (1983).

29. **L. Wu, X. Wang, and L. Li**: Lead-free $BaTiO_3$–$Bi(Zn_{2/3}Nb_{1/3})O_3$ weakly coupled relaxor ferroelectric materials for energy storage. *RSC Adv.* **6**, 14273–14282 (2016).

30. **K. Uchino and S. Nomura**: Critical exponents of the dielectric constants in diffused phase-transition crystals. *Ferroelectrics* **44**, 55–61 (1982).

31. **X. Diez-Betriu, J.E. Garcia, C. Ostos, A.U. Boya, D.A. Ochoa, L. Mestres, and R. Perez**: Phase transition characteristics and dielectric properties of rare-earth (La, Pr, Nd, Gd) doped $Ba(Zr_{0.09}Ti_{0.91})O_3$ ceramics. *Mater. Chem. Phys.* **125**, 493–499 (2011).

32. **S. Anwar, P.R. Sagdeo, and N.P. Lalla**: Crossover from classical to relaxor ferroelectrics in $BaTi_{1−x}Hf_xO_3$ ceramics. *J. Phys.: Condens. Matter* **18**, 3455–3468 (2006).

33. **C. Ang, Z. Jing, and Z. Yu**: Ferroelectric relaxor $Ba(TiCe)O_3$. *J. Phys.: Condens. Matter* **14**, 8901–8912 (2002).

34. **H. Du, W. Zhou, F. Luo, D. Zhu, S. Qu, and Z. Pei**: Phase structure, dielectric properties, and relaxor behavior of $(K_{0.5}Na_{0.5})NbO_3$–$(Ba_{0.5}Sr_{0.5})TiO_3$ lead-free solid solution for high temperature applications. *J. Appl. Phys.* **105**, 124104–124109 (2009).

35. **T. Badapanda, S.K. Rout, L.S. Cavalcante, J.C. Sczancoski, S. Panigrahi, E. Longo, and M.S. Li**: Optical and dielectric relaxor

behaviour of Ba(Zr$_{0.25}$Ti$_{0.75}$)O$_3$ ceramic explained by means of distorted clusters. *J. Phys. D: Appl. Phys.* **42**, 175414–175422 (2009).

36. G. Jug: Critical behavior of disordered spin systems in two and three dimensions. *Phys. Rev. B* **27**, 609–612 (1983).

37. H. Reiger: Critical behavior of the three-dimensional random-field Ising model: Two-exponent scaling and discontinuously transition. *Phys. Rev. B* **52**, 6659–6667 (1995).

38. W. Kleemann, J. Dec, P. Lehnen, R. Blinc, B. Zalar, and R. Pankrath: Uniaxial relaxor ferroelectrics: The ferroic random-field Ising model materialized at last. *Europhys. Lett.* **57**, 14–19 (2002).

39. H. Vogel: Das temperature-abhangigkeitsgesetz der Viskositat von Flussigkeiten (the law of viscosity change with temperature). *Z. Phys.* **22**, 645–646 (1922).

40. G.S. Fulcher: Analysis of recent measurements of the viscosity of glasses. *J. Am. Ceram. Soc.* **8**, 339–355 (1925).

41. H. Ogihara, C.A. Randall, and S. Trolier-McKinstry: Weakly coupled relaxor behavior of BaTiO$_3$–BiScO$_3$ ceramics. *J. Am. Ceram. Soc.* **92**, 110–118 (2009).

42. Y. Moriya, H. Kawaji, T. Tojo, and T. Atake: Specific-heat anomaly caused by ferroelectric nanoregions in Pb(Mg$_{1/3}$Nb$_{2/3}$)O$_3$ and Pb(Mg$_{1/3}$Ta$_{2/3}$)O$_3$ relaxors. *Phys. Rev. Lett.* **90**, 205901–205904 (2003).

43. N. Novak, R. Pirc, M. Wencka, and Z. Kutnjak: High-resolution calorimetric study of Pb(Mg$_{1/3}$Nb$_{2/3}$)O$_3$ single crystal. *Phys. Rev. Lett.* **109**, 037601 (2012).

44. S. Nayak, K. Dasari, D.C. Joshi, P. Pramanik, R. Palai, A. Waske, R.N. Chauhan, N. Tiwari, T. Sarkar, and S. Thota: Low-temperature anomalous magnetic behavior of Co$_2$TiO$_4$ and Co$_2$SnO$_4$. *J. Appl. Phys.* **120**, 163905–163910 (2016).

45. J. Rodríguez-Carvajal: *Study of Micro-structural Effects by Powder Diffraction Using the Program FULLPROF* (Laboratoire Le' on Brillouin (CEA-CNRS), France, 2006).

46. M. Manikandan, T. Tanabe, P. Li, S. Ueda, G.V. Ramesh, R. Kodiyath, J. Wang, T. Hara, A. Dakshanamoorthy, S. Ishihara, K. Ariga, J. Ye, N. Umezawa, and H. Abe: Photocatalytic water splitting under visible light by mixed-valence Sn$_3$O$_4$. *Appl. Mater. Interfaces* **6**, 3790–3793 (2014).

47. Y.M. Vysochanskii, D. Baltrunas, A.A. Grabar, K. Mazeika, K. Fedyo, and A. Sudavicius: Mössbauer ^{119}Sn and XPS spectroscopy of Sn$_2$P$_2$S$_6$ and SnP$_2$S$_6$ crystals. *Phys. Status Solidi B* **246**, 1110–1117 (2009).

48. T. Egami and S.J.L. Billinge: *Underneath the Bragg Beaks: Structural Analysis of Complex Materials* (Pergamon Press, Oxford, UK, 2003).

49. I.K. Jeong, T.W. Darling, J.K. Lee, T. Proffen, R.H. Heffner, J.S. Park, K.S. Hong, W. Dmowski, and T. Egami: Direct observation of the formation of polar nanoregions in PbMg1/3Nb2/3O3 using neutron pair distribution function analysis *Phys. Rev. Lett.* **94**, 147602–147605 (2005).

50. J.S.O. Evans: Advanced input files & parametric quantitative analysis using topas. *Mater. Sci. Forum.* **651**, 1–9 (2010).

51. A.A. Coelho, P.A. Chater, and A. Kern: Fast synthesis and refinement of the atomic pair distribution function *J. Appl. Crystallogr.* **48**, 869–875 (2015).

52. B. Jaffe: *Piezoelectric Ceramics*, 1st ed. (Academic Press, London, UK, 1971); ISBN: 9780323155687.

53. T-M. Usher, T. Iamsasri, J.S. Forrester, N. Raengthon, N. Triamnak, D.P. Cann, and J.L. Jones: Local and average structures of BaTiO$_3$-Bi(Zn$_{1/2}$Ti$_{1/2}$) *J. Appl. Phys.* **120**, 184102–184114 (2016).

54. J.F. Scott: Electrocaloric materials. *Annu. Rev. Mater. Res.* **41**, 229–240 (2011).

55. C.R. Bowen, J. Taylor, E. LeBoulbar, D. Zabek, A. Chauhan, and R. Vaish: Pyroelectric materials and devices for energy harvesting applications. *Energy Environ. Sci.* **7**, 3836 (2014).

56. M. Sanlialp, V.V. Shvartsman, M. Acosta, and D.C. Lupascu: Electrocaloric effect in Ba(Zr,Ti)O$_3$–(Ba,Ca)TiO$_3$ ceramics measured directly. *J. Am. Ceram. Soc.* **99**, 4022–4030 (2016).

57. M. Valant: Electrocaloric materials for future solid-state refrigeration technologies. *Prog. Mater. Sci.* **57**, 980–1009 (2012).

58. F.L. Goupil, A. Berenov, A.K. Axelsson, M. Valant, and N.M. Alford: Direct and indirect electrocaloric measurements on ⟨001⟩-PbMg$_{1/3}$Nb$_{2/3}$O$_3$–30PbTiO$_3$ single crystals. *J. Appl. Phys.* **111**, 124109 (2012).

59. C. Molin, M. Sanlialp, V.V. Shvartsman, D.C. Lupascu, P. Neumeister, A. Schönecker, and S. Gebhardt: Effect of dopants on the electrocaloric effect of 0.92 Pb(Mg$_{1/3}$Nb$_{2/3}$)O$_3$ 0.08PbTiO$_3$ ceramics. *J. Eur. Ceram. Soc.* **35**, 2065–2071 (2015).

60. F.L. Goupil, J. Bennett, A-K. Axelsson, M. Valant, A. Berenov, A.J. Bell, T.P. Comyn, and N.M. Alford: Electrocaloric enhancement near the morphotropic phase boundary in lead-free NBT-KBT ceramics. *Appl. Phys.Lett.* **107**, 172903 (2015).

61. N. Novak, Z. Kutnjak, and R. Pirc: High-resolution electrocaloric and heat capacity measurements in barium titanate. *Europhys. Lett.* **103**, 47001 (2013).

62. F. Weyland, R. Perez-Moyet, G.A. Rossetti, Jr., and N. Novak: Material measures of electrocaloric cooling power in perovskite ferroelectrics. *Energy Technol.* **6**, 1512–1518 (2018).

63. A.S. Mischenko, Q. Zhang, R.W. Whatmore, J.F. Scott, and N.D. Mathur: Giant electrocaloric effect in the thin film relaxor ferroelectric 0.9 PbMg$_{1/3}$Nb$_{2/3}$O$_3$–0.1PbTiO$_3$ near room temperature. *Appl. Phys. Lett.* **89**, 242912 (2006).

64. H. Yao, K. Ema, and C.W. Garland: Nonadiabatic scanning calorimeter. *Rev. Sci. Instrum.* **69**, 172–178 (1998).

65. X. Qiu, J.W. Thompson, and S.J.L. Billinge: PDFgetX2: A GUI driven program to obtain the pair distribution function from X-ray powder diffraction data. *J. Appl. Crystallogr.* **37**, 678 (2004).